Optics Communications 439 (2019) 260–269

Contents lists available at ScienceDirect

Optics Communications

journal homepage: www.elsevier.com/locate/optcom

Time-averaged computer generated holography for the estimation of torsional amplitudes of oscillating microdevices

Paulius Palevicius [a,*], Loreta Saunoriene [a], Maosen Cao [b], Minvydas Ragulskis [a,b]

[a] Department of Mathematical Modeling, Kaunas University of Technology, Kaunas, Lithuania
[b] Department of Engineering Mechanics, Hohai University, Nanjing, Jiangsu 210098, China

ARTICLE INFO

Keywords:
Time-averaged moiré
MEMS
Sensors
CGH

ABSTRACT

Time-averaged geometric moiré technique has been applied in various areas including experimental interpretation of moiré patterns in order to determine the amplitudes of the oscillations of microdevices and inverse moiré pattern synthesis for construction of dynamic visual cryptography schemes. Another common component in optical setups are diffractive optical elements. Computational algorithms can be used to design diffractive optical elements in the form of a computer generated hologram of a nonexistent, synthetic or even a virtual object. The main goal of this paper is to demonstrate the feasibility of the optical scheme based on the integration of time-averaged geometric moiré and computer generated holography. We present the design of the optical setup, derive the equations governing the formation of time-averaged fringes in the optical projection plane and validate the results by performing computational simulations of the formation of time-averaged fringes when torsional oscillations are performed. This approach has promising applications as an optical scale for the quantitative estimation of the amplitude of torsional oscillations as well as the validation of microdevices when the amplitude of torsional oscillations experience fluctuations due to environmental conditions and degradation.

1. Introduction

Geometric moiré [1,2] is a classical and widely used whole-field opto-mechanical experimental technique. Geometric moiré is based on the analysis of visual patterns produced by the superposition of two regular gratings and the geometric interference of these gratings. A common moiré grating is an array of alternating transparent and opaque straight lines. However, experimental applications exploiting concentric circles, cross-gratings, regular arrays of dots or even randomly distributed dots can be found in the engineering literature [3,4]. Common moiré techniques are double-exposure moiré, projection moiré, time-averaged moiré [1]. Two basic goals exist in the geometric moiré pattern analysis. The first goal is oriented towards the experimental interpretation of moiré patterns for the determination of deformations (at the centerlines of moiré fringes). It has been shown, that time-averaged moiré can be exploited for in-plane vibrational analysis [5] and degradation prediction of mechanical components performing angular oscillations [6]. Another objective is the synthesis of inverse moiré patterns when one has to generate such a moiré grating which yields the required pattern [2,7].

Time-averaged moiré has been employed for the construction of novel visual cryptography schemes. Visual cryptography [8–10] is a cryptographic technique that encrypts visual information in such a way that the decryption is a completely mechanical operation that can be performed without an aid of the computer. Synthesis of a predefined pattern of time-averaged fringes enables the construction of special image hiding techniques (when the secret image is leaked in the form of a pattern of time-averaged moiré fringes in a time-averaged cover image performing harmonic oscillations) [11]. This secret image is embedded into a single cover stochastic moiré grating. This approach enables to construct visual cryptography schemes that do not require multiple shares, such as an optical image hiding scheme based on chaotic vibration of a deformable moiré grating [12] and an image hiding scheme based on time-averaged elliptic oscillations [13].

Diffractive optical elements (DOEs) that modify wavefronts by segmenting and redirecting the segments through the use of the interference and the phase control are employed in this paper. DOEs are used in various optical setups in order to modify and control the shape of the laser beam and can be used as a replacement for the refractive optics such as optical lenses, spheres, and prisms [14]. A commonly used DOEs are computer generated holograms (CGHs). CGH is a mature technology for shaping the amplitude and the phase of a light wave [15]. CGH is different from an optical hologram in the sense that computational algorithms are used to design a CGH of a nonexistent, synthetic or even a virtual object, thus there is no need to use real objects in the recording stage and the functionality of a DOE can be optimized mathematically rather than experimentally [16]. Different

* Corresponding author.
E-mail address: paulius.palevicius@ktu.lt (P. Palevicius).

https://doi.org/10.1016/j.optcom.2019.01.072
Received 20 December 2018; Received in revised form 23 January 2019; Accepted 25 January 2019
Available online 31 January 2019
0030-4018/

methods are used to manufacture DOEs and CGHs including half-tone masking, diamond turning, electron or ion beam writing [16–19]. These techniques have matured from microelectronics in general and MEMS micro-fabrication in particular. The most popular algorithms for the computation of an estimate of the phase hologram are classical iterative Fourier transform algorithms such as Gerchberg–Saxton algorithm [20] or adaptive–additive algorithm [21]. The latter is used in our paper for the computation of the phase data of CGHs.

The main goal of this paper is to present the optical setup applicable for measurement of MEMS components performing torsional oscillations. Such optical technique is directly applicable for scanning micro-mirror devices where mirror plate is performing oscillations around the torsional axis [22–24], gyroscopes and resonant accelerometers [25], magnetometers [26], and mass detection devices [27]. The proposed optical setup is implemented by integrating two different optical techniques: time-averaged geometric moiré and CGH. The uniqueness of the proposed optical technique is first of all based on the fact that MEMS components performing torsional oscillations are too small for the direct application of time-averaged fringed-based optical measurement techniques — but the objective of this paper is to present an optical technique capable to measure out-of-plane torsional oscillations of MEMS components in the time-average mode. Therefore, the presented optical technique must overcome this limitation and still be capable to register time-averaged fringes induced by torsional oscillations of MEMS components. The optical scheme is constructed in such a way, that different amplitudes of torsional oscillations of MEMS components yield fringes at different locations on the projection plane. As mentioned previously, the formation of a CGH on the surface of a MEMS component can be accomplished by micro-fabrication techniques. However, standard CGH applications are limited by the formation of static target images in the projection plane. The originality of the presented optical setup is based on a two step strategy for the formation of time-averaged moiré fringes in the projection plane. First of all a CGH is used to form a static image of the moiré grating in the projection plane (when the MEMS component is in a stationary mode). Secondly, the optical setup is adjusted in such a way, that torsional oscillations of the MEMS component result into an oscillating moiré grating in the projection plane. This is in stark contrast to existing direct optical techniques, such as static deformation analysis of MEMS components [28], which are not applicable for optical assessment of vibrating MEMS components.

The proposed scheme can be exploited for the construction of an optical scale for the measurement of the amplitude of torsional oscillations. Moreover, this approach has its applications as an optical sensor system for the validation of microdevices when the amplitude of torsional oscillations experience fluctuations due to changing environmental conditions or mechanical degradation.

This paper is organized as follows. Optical background describing the formation of time-averaged moiré fringes and CGH is discussed in Section 2. The virtual optical setup and optical relationships for MEMS components performing torsional oscillations is given in Section 3. The results of computational simulations are given in Section 4. Concluding remarks are presented in the final Section.

2. Preliminaries

The optical setup that we propose in this paper is based on two optical techniques — time-averaged geometric moiré and CGH. This section provides the main optical relationships governing the formation of one-dimensional time-averaged fringes. Furthermore, the adaptive–additive algorithm which is used for the computation of the phase data of CGHs is described.

2.1. Time-averaged geometric moiré

Moiré grating on the one-dimensional non-deformable surface in the state of equilibrium can be interpreted as a harmonic function (Fig. 1(a)) [1]:

$$F_1(x) = \frac{1}{2} + \frac{1}{2}\cos\left(\frac{2\pi}{\lambda}x\right), \tag{1}$$

where x is the longitudinal coordinate; $F_1(x)$ is the intensity of a grayscale color at point x; λ is the pitch of the harmonic grating. Values 0 and 1 of function $F_1(x)$ correspond to black and white colors respectively; intermediate values represent an appropriate grayscale color (Fig. 1(b)).

Without losing the generality let us assume a linear field of deformations $u = \pm kx$, where k is a real positive number. Additive superposition of the moiré gratings in the states of the maximal opposite deformations ($u = -kx$ and $u = kx$) lead to the formation of the pattern of fringes of double exposure geometric moiré [2]:

$$\begin{aligned} F_d(x) &= \frac{1}{2} + \frac{1}{4}\left(\cos\left(\frac{2\pi x}{\lambda(1+k)}\right) + \cos\left(\frac{2\pi x}{\lambda(1-k)}\right)\right) \\ &= \frac{1}{2} + \frac{1}{2}\cos\left(\frac{2\pi x}{\lambda\left(1-k^2\right)}\right)\cos\left(\frac{2\pi k x}{\lambda\left(1-k^2\right)}\right). \end{aligned} \tag{2}$$

When k is a small number, the envelope function modulating the regular beating process reads: $\frac{1}{2} + \frac{1}{2}\cos\left(\frac{2\pi k x}{\lambda(1-k^2)}\right)$. This pattern is depicted in parts (c) and (d) of Fig. 1.

Double exposure geometric moiré techniques can be extended to time-average geometric moiré method. Let us assume that deflections from the state of equilibrium oscillate in time and are defined as:

$$u(t) = a\sin(\omega t + \phi), \tag{3}$$

where a is the amplitude of harmonic oscillations; ω is the angular frequency; ϕ is the phase. The time-averaged signal (when the exposure time T tends to infinity) is expressed as [1]:

$$\begin{aligned} F_t(x) &= \lim_{T\to\infty}\frac{1}{T}\int_0^T F_1(x - a\sin(\omega t + \phi))\,dt \\ &= \frac{1}{2} + \frac{1}{2}\cos\left(\frac{2\pi}{\lambda}x\right)J_0\left(\frac{2\pi}{\lambda}a\right). \end{aligned} \tag{4}$$

where J_0 is the zero order Bessel function of the first kind:

$$J_0(x) = \lim_{T\to\infty}\frac{1}{T}\int_0^T \exp(i\cdot x\sin(\omega t + \phi))\,dt. \tag{5}$$

Graphical representations of Eq. (4) are shown in Fig. 1(e) and (f) respectively. The envelope function modulating the time-averaged blur induced by harmonic oscillations reads:

$$E(a) = \frac{1}{2} \pm \frac{1}{2}J_0\left(\frac{2\pi}{\lambda}a\right). \tag{6}$$

Thus, time-averaged moiré fringes do form when

$$J_0\left(\frac{2\pi}{\lambda}a\right) = 0. \tag{7}$$

The relationship between the sequential number of time-averaged fringe, the amplitude of harmonic oscillations and the pitch of the moiré grating reads:

$$\frac{2\pi}{\lambda}a_i = r_i, \tag{8}$$

where r_i denotes the ith root of J_0; a_i is the amplitude of oscillation at the center of the ith time-averaged fringe. Graphical representation of the relationship in Eq. (8) is depicted in Fig. 2(a) and (b). It is clear that time-averaged fringes do form at amplitudes $a_i = \frac{\lambda}{2\pi}r_i$. Vertical dashed lines in Fig. 2 interconnect centers of time-averaged fringes located at roots of J_0.

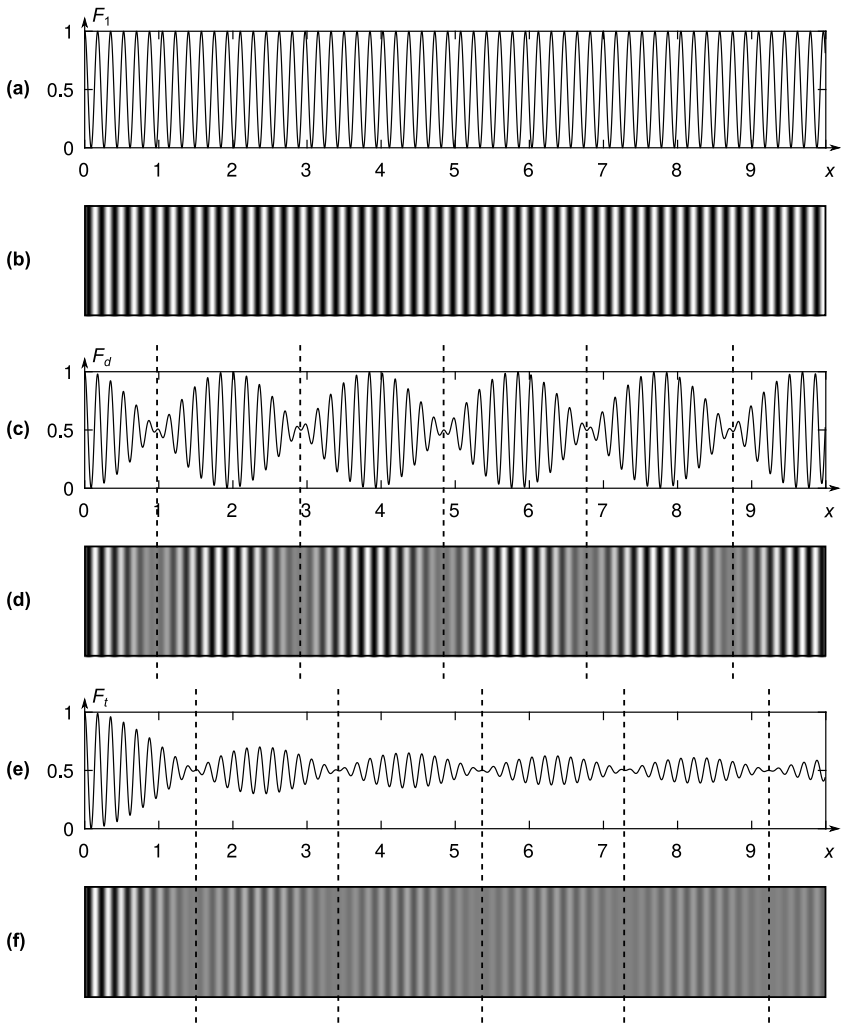

Fig. 1. Optical representation of one-dimensional geometric moiré at $\lambda = 0.175$: (a) Variation of the grayscale color of the moiré grating in the state of equilibrium. (b) Graphical representation of part (a). (c)–(d) Double-exposure geometric moiré in case of two maximal opposite deformations and its graphical representation at $u = kx$; $k = 0.045$. (e)–(f) Variation of the grayscale color in the time-averaged image.

2.2. Adaptive–additive algorithm

This section provides the basic steps of the adaptive–additive algorithm [21] for the estimation of the phase field. This algorithm reconstructs the spatial frequency phase (k-space) for a desired intensity in the image plane (x-space). Assume the amplitude in k-space is defined as A_0 and the starting phase of the wave in k-space is defined as ϕ_n^k. The first step is to combine A_0 with ϕ_n^k and to apply the Fourier transformation in order to transform the wave in the spatial frequency phase to the image plane space:

$$A_0 e^{i\phi_n^k} \xrightarrow{FFT} A_n^f e^{i\phi_n^f}. \tag{9}$$

Then the resulting reconstructed image I_n^f is compared to the expected image I_0^f:

$$\varepsilon = \sqrt{\left(I_n^f\right)^2 - \left(I_0\right)^2}, \tag{10}$$

where $I_n^f = \left(A_n^f\right)^2$. The decision to terminate the iterative process is made based on the value of error ε and the convergence requirements. If the iterative process is continued, the transformed amplitude A_n^f is mixed with the desired amplitude A^f:

$$\bar{A}_n^f = \left[\alpha A^f + (1-\alpha) A_n^f\right], \tag{11}$$

where α is the mixing ratio ($0 \le \alpha \le 1$) and $A^f = \sqrt{I_0}$. The next step results into the combination of $\bar{A}_n^f$ with the x-space phase and the application of the inverse Fourier transform:

$$\bar{A}^f e^{i\phi_n^f} \xrightarrow{iFFT} \bar{A}_n^k e^{i\phi_n^k}. \tag{12}$$

Finally, $\bar{A}_n^k$ and ϕ_n^k are separated and the process is repeated.

Note, that the adaptive–additive algorithm transforms into the Gerchberg–Saxton algorithm at $\alpha = 1$. On the other hand, $\bar{A}_n^k = A_0$ at $\alpha = 0$.

3. Optical relationships and methodology

We propose the optical scheme that enables the estimation of torsional amplitude of microdevices performing torsional oscillations. The virtual optical setup and mathematical relationships governing the formation of time-averaged moiré fringes when the object is performing torsional oscillations are presented in the following subsections.

3.1. The optical setup

The virtual optical setup is given in Fig. 3. The MEMS component performing torsional oscillations is shown in Fig. 3 part (a). MEMS devices that can be considered for application of the proposed technique are (but not limited to) micro-mirrors, gyroscopes, resonant accelerometers,

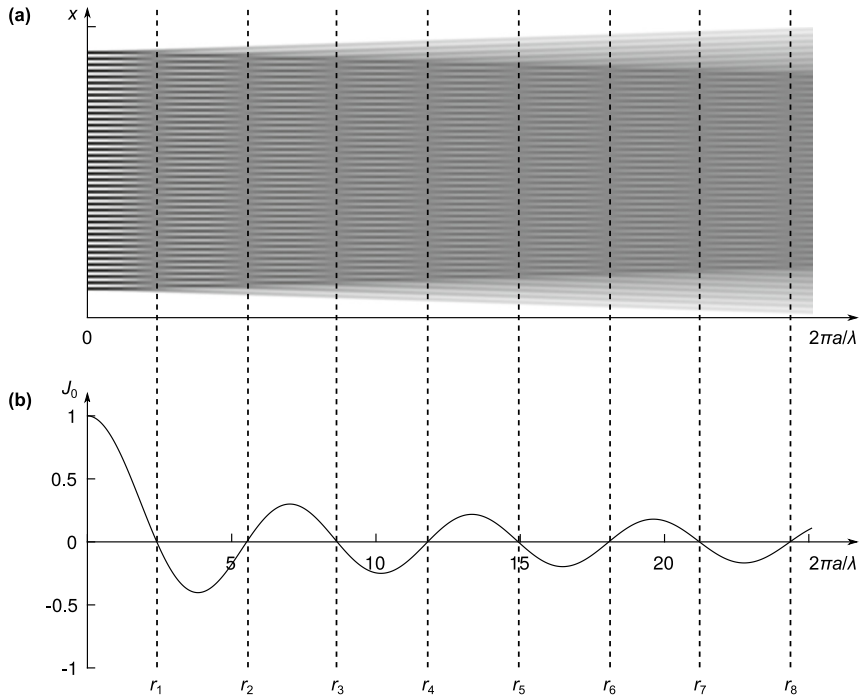

Fig. 2. Graphical illustration of Eq. (8) at $\lambda = 0.25$: (a) One-dimensional time-averaged geometric moiré at increasing amplitudes of harmonic oscillations; (b) The envelope function of the time-averaged moiré signal (Eq. (6)). Vertical dashed lines interconnect centers of time-averaged fringes with roots of J_0.

magnetometers, and mass detection sensors. Such devices should have an additional layer of DOE in a form of a CGH that is applied on one of its surfaces. Moreover, DOE has to be implemented in the form of a reflecting mirror. Coherent laser source is shown in Fig. 3 part (b). The projection plane with an aperture for a laser beam is shown in Fig. 3 part (c). The size of the aperture should be selected according to the dimension of the illuminated DOE; the beam expander [29] first expands and then collimates the laser beam (Fig. 3). The illumination of the DOE element by laser beam results in the formation of the target image in the projection plane due to the diffraction from the surface of the CGH. The rectangular target image containing the moiré grating in the state of equilibrium is shown in Fig. 3 part (d).

The laser beam has to be parallel to the normal direction of the projection plane and to the normal direction of DOE element in the state of equilibrium. Alternatively, it is possible to eliminate the aperture from the projection plane by illuminating the DOE from a different angle. In that case modifications have to be applied in the design step of the DOE to the desired image in such a way that non-parallel illumination of the DOE would result into a rectangular target image in the projection plane [30].

3.2. The formation of time-averaged moiré fringes in 1D

Let us consider the optical scheme in xOz plane (Fig. 4). One-dimensional moiré grating is analyzed in the projection plane. The coordinate of the ith point at time moment $t = 0$ reads:

$$x_i(0) = L\tan(\alpha_i), \tag{13}$$

where α_i is the angle between the incident laser beam and the direction from the DOE towards the ith point on the Ox axis (Fig. 4(a)). The coordinate of the ith point at time moment t reads (Fig. 4(b)):

$$x_i(t) = L\tan(\alpha_i + \beta\sin\omega t), \tag{14}$$

where β is the amplitude of the torsional oscillation; ω is the angular frequency of the torsional oscillation of the MEMS component.

Note that $\alpha_i = \arctan\left(\frac{x_i(0)}{L}\right)$. Then Eq. (14) can be rearranged as follows:

$$x_i(t) = \frac{x_i(0) + L\tan(\beta\sin\omega t)}{1 - \frac{x_i(0)}{L}\tan(\beta\sin\omega t)}. \tag{15}$$

The moiré grating in the state of equilibrium at point x_i takes the following form (Fig. 5(a)):

$$F_1(x_i(0)) = \frac{1}{2} + \frac{1}{2}\cos\left(\frac{2\pi}{\lambda}x_i(0)\right). \tag{16}$$

The moiré grating in the deformed state at point x_i and at time moment t reads [12,31]:

$$F_2(x_i(t)) = \frac{1}{2} + \frac{1}{2}\cos\left(\frac{2\pi}{\lambda}x_i(0)\right). \tag{17}$$

Fig. 5(b) and 5(c) correspond to moiré gratings in case of maximal torsional deformations from the state of equilibrium (the angle of torsional deflections is β in part (b) and $-\beta$ in part (c)).

Note that Eq. (17) is implicit because $x_i(t)$ depends upon $x_i(0)$ (Eq. (15)). In order to rewrite Eq. (17) in the explicit form we need to solve $x_i(0)$ as a function of z_i from the relationship $x_i(t) = z_i$ [31]:

$$\frac{x_i(0) + L\tan(\beta\sin\omega t)}{1 - \frac{x_i(0)}{L}\tan(\beta\sin\omega t)} = z_i. \tag{18}$$

The explicit solution reads:

$$x_i(0) = \frac{z_i - L\tan(\beta\sin\omega t)}{1 + \frac{z_i}{L}\tan(\beta\sin\omega t)}. \tag{19}$$

Finally, the deformed moiré grating at time moment t at point x can be expressed as follows:

$$F_2(x,t) = \frac{1}{2} + \frac{1}{2}\cos\left(\frac{2\pi}{\lambda}\left(\frac{x - L\tan(\beta\sin\omega t)}{1 + \frac{x}{L}\tan(\beta\sin\omega t)}\right)\right). \tag{20}$$

If the moiré grating oscillates in time, the time-averaged moiré signal reads:

$$F_t(x) = \lim_{T\to\infty}\frac{1}{T}\int_0^T F_2(x,t)dt \tag{21}$$

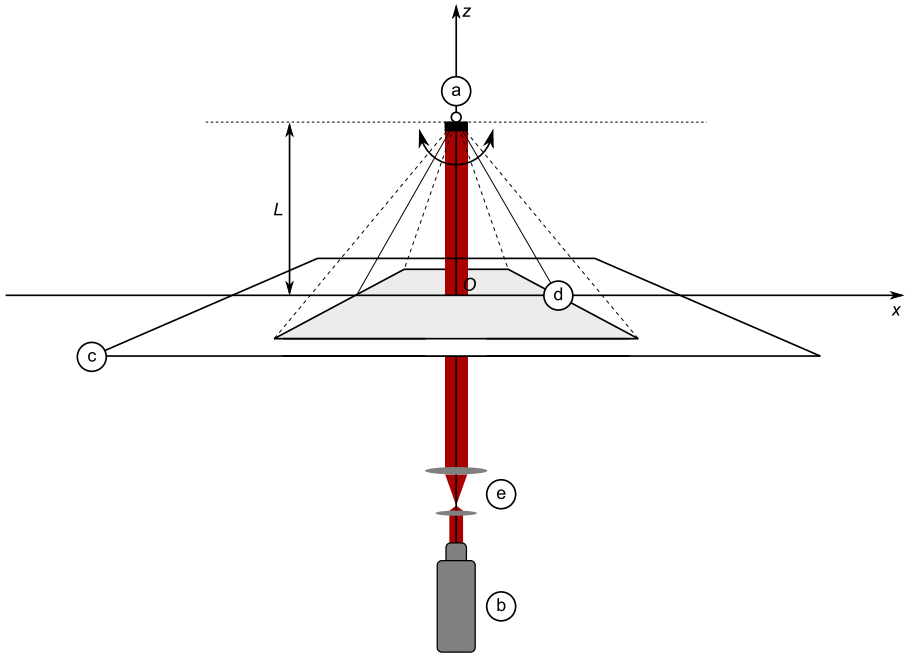

Fig. 3. The schematic diagram of the optical setup for the proposed optical scheme: (a) The MEMS component with DOE layer performing torsional oscillations. (b) The laser source. (c) The projection plane. (d) The target image of moiré grating on the projection plane in the state of equilibrium. (e) The beam expander.

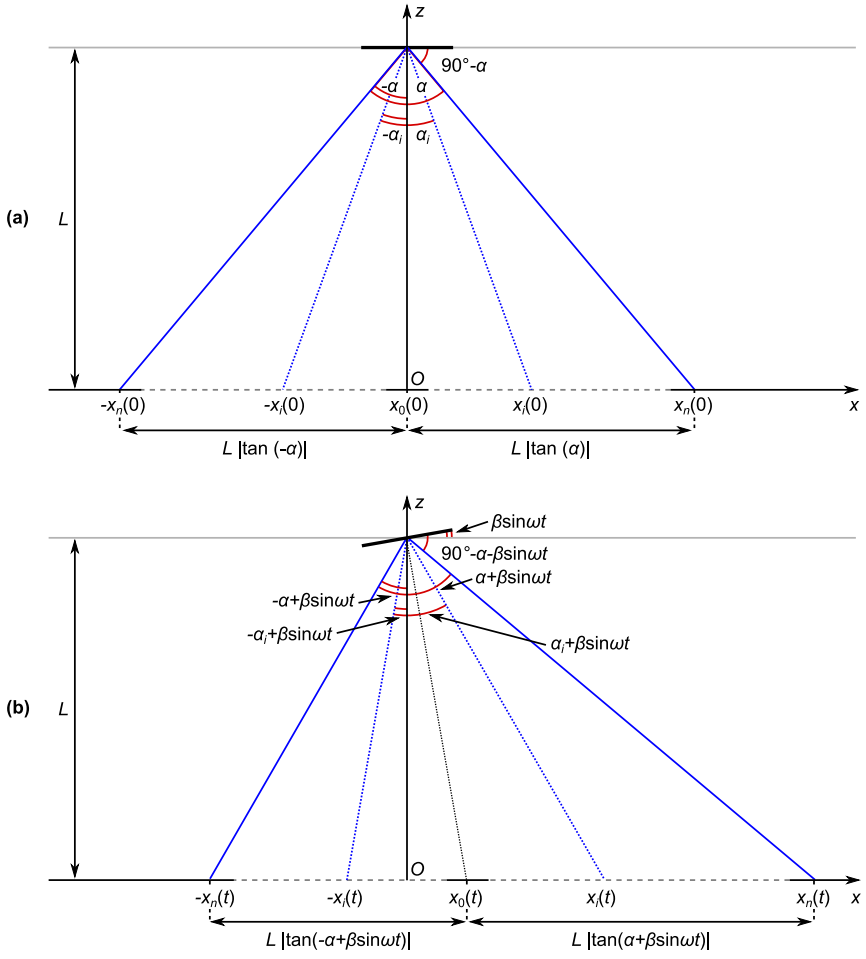

Fig. 4. Graphical representation of the optical scheme in the xOz plane: (a) The formation of the one-dimensional moiré grating in the state of equilibrium. (b) The formation of the one-dimensional moiré grating at time moment t. The angle β is the amplitude of harmonic torsional oscillations.

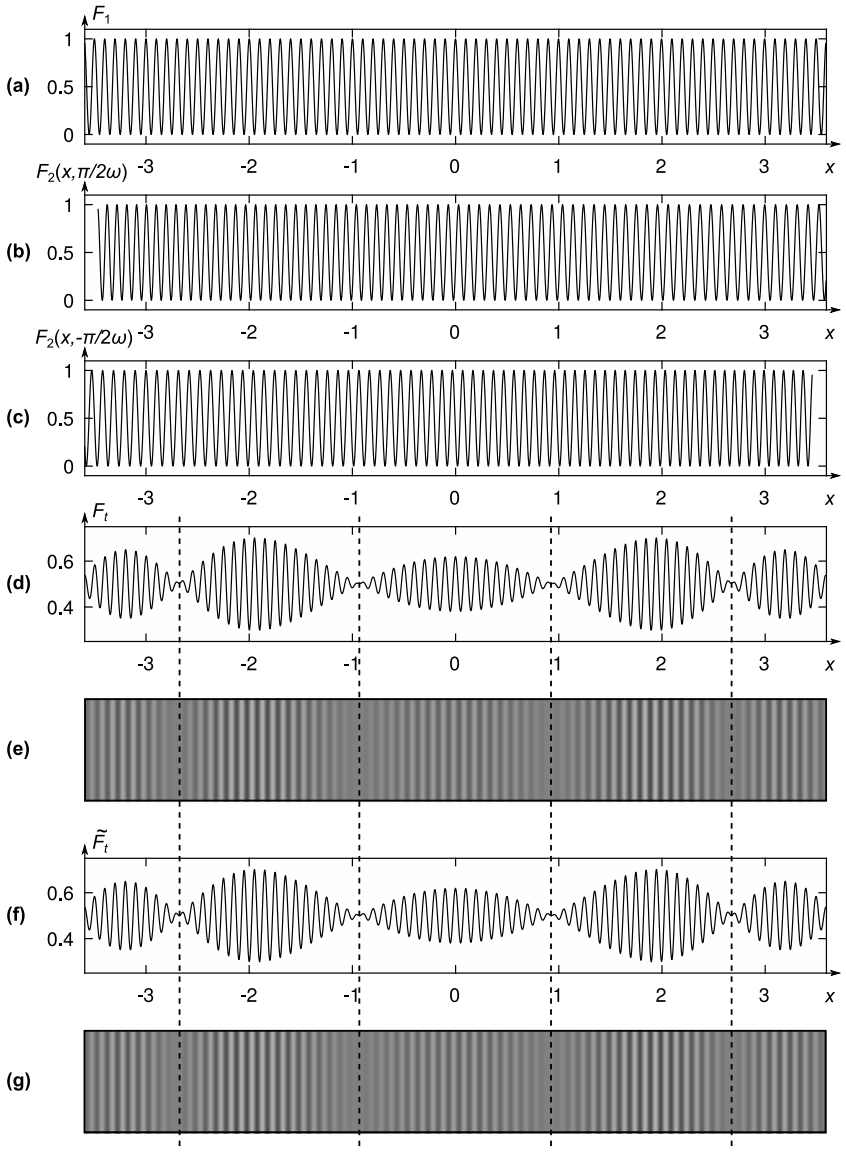

Fig. 5. The formation of time-averaged fringes at $L = 2$, $\alpha = \frac{\pi}{3}$, $\lambda = 0.1$, $\beta = \frac{\pi}{200}$: (a) The stationary moiré grating. (b)–(c) Moiré gratings at maximal torsional deflections at β and $-\beta$ respectively. (d)–(e) The time-averaged moiré grating calculated according to Eq. (21) and its graphical representation. (f)–(g) The time-averaged moiré grating calculated according to the approximated equation (Eq. (26)) and its graphical representation. Black dashed lines throughout (d)–(g) indicate the centers of time-averaged fringes.

$$= \frac{1}{2} + \lim_{T\to\infty}\frac{1}{2T}\int_0^T \cos\left(\frac{2\pi}{\lambda}\left(\frac{x - L\tan(\beta\sin\omega t)}{1 + \frac{x}{L}\tan(\beta\sin\omega t)}\right)\right)dt. \tag{22}$$

The time-averaged moiré grating calculated according to Eq. (21) is illustrated in Fig. 5(d); Fig. 5(e) corresponds to the graphical representation of Fig. 5(d). It is clear that the pattern of time-averaged fringes emerges in Fig. 5(e). However, the derivation of the analytic relationship between the coordinates of the centers of time-averaged fringes and the angle of the torsional deflection β requires integration of the integral in Eq. (21). Unfortunately, this integral cannot be expressed in closed form. We will demonstrate that an approximated relationship can be derived for the calculation of the time-averaged moiré in Eq. (21).

Note that the argument of the cosine function in Eq. (21) can be rearranged as follows [12]:

$$\begin{aligned}\frac{x - L\tan(\beta\sin\omega t)}{1 + \frac{x}{L}\tan(\beta\sin\omega t)} &\approx (x - L\tan(\beta\sin\omega t))\left(1 - \frac{x}{L}\tan(\beta\sin\omega t)\right) + O\left(x^2\right)\\ &= x + x\tan^2(\beta\sin\omega t)\\ &\quad - \left(\frac{x^2}{L} + L\right)\tan(\beta\sin\omega t) + O\left(x^2\right)\\ &= \Phi + \Psi + O\left(x^2\right),\end{aligned} \tag{23}$$

where $\Phi = x + x\tan^2(\beta\sin\omega t)$ and $\Psi = \left(\frac{x^2}{L} + L\right)\tan(\beta\sin\omega t)$.

Therefore, the time-averaged moiré grating reads:

$$\begin{aligned}\tilde{F}_t(x) &\approx \frac{1}{2} + \lim_{T\to\infty}\frac{1}{2T}\int_0^T \cos\left(\frac{2\pi}{\lambda}(\Phi - \Psi)\right)dt\\ &= \frac{1}{2} + \lim_{T\to\infty}\frac{1}{2T}\int_0^T \cos\left(\frac{2\pi}{\lambda}\Phi\right)\cos\left(\frac{2\pi}{\lambda}\Psi\right)dt\\ &\quad + \lim_{T\to\infty}\frac{1}{2T}\int_0^T \sin\left(\frac{2\pi}{\lambda}\Phi\right)\sin\left(\frac{2\pi}{\lambda}\Psi\right)dt.\end{aligned} \tag{24}$$

However, if β is a sufficiently small number, then $\tan(\beta\sin\omega t) \approx \beta\sin\omega t$. Moreover, $\sin\left(\frac{2\pi}{\lambda}\Phi\right) = \sin\left(\frac{2\pi}{\lambda}x\right) + O\left(\beta^2\right)$ and $\cos\left(\frac{2\pi}{\lambda}\Phi\right) = \cos\left(\frac{2\pi}{\lambda}x\right) + O\left(\beta^2\right)$. Due to the oddness of the sine and the tangent

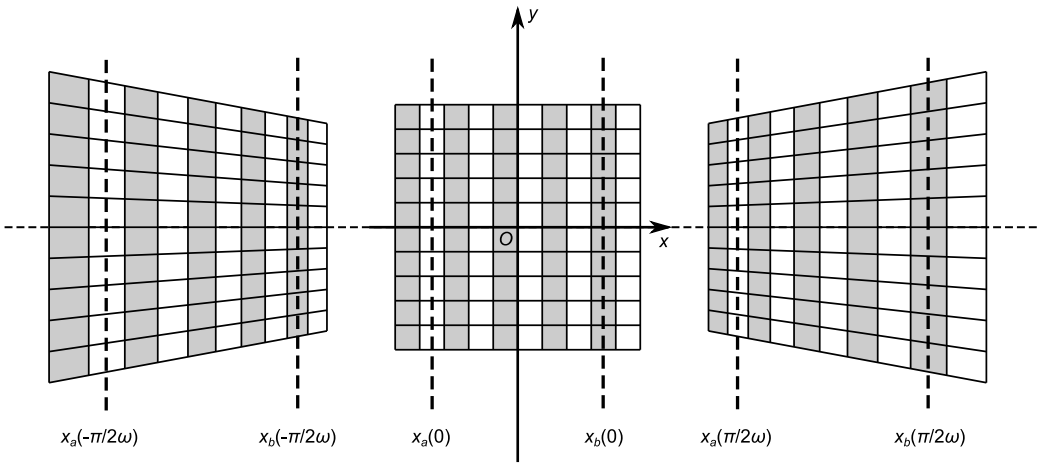

Fig. 6. The constitutive lines of the moiré grating remain straight in the projection plane. The deformation of the target image in the projection plane. The target image containing the 2D moiré grating in the state of equilibrium is shown in the middle. Target images in states of maximal torsional deflections of the MEMS component are depicted on the left and on the right sides.

functions the following equality holds true:

$$\lim_{T\to\infty}\frac{1}{T}\int_0^T \sin\left(\frac{2\pi}{\lambda}\Psi\right)dt = 0. \tag{25}$$

Finally,

$$\begin{aligned}\tilde{F}_t(x) &\approx \frac{1}{2} + \lim_{T\to\infty}\frac{1}{2T}\int_0^T \cos\left(\frac{2\pi}{\lambda}\Phi\right)\cos\left(\frac{2\pi}{\lambda}\Psi\right)dt \\ &\approx \frac{1}{2} + \frac{1}{2}\cos\left(\frac{2\pi}{\lambda}x\right)J_0\left(\frac{2\pi}{\lambda}\left(\frac{x^2}{L}+L\right)\beta\right).\end{aligned} \tag{26}$$

The resulting approximation (Eq. (26)) yields an original explicit quadratic relationship between the center of a time-averaged fringe and the amplitude of torsional out-of-plane oscillations. The time-averaged image becomes uniformly gray at the roots of J_0 (at $\frac{2\pi}{\lambda}\frac{\beta}{L}\left(x^2+L^2\right)=r_i$), therefore equation

$$x = \pm\sqrt{r_i\frac{\lambda L}{2\pi\beta} - L^2}, \quad r_i \geq \frac{2\pi\beta L}{\lambda} \tag{27}$$

describes the location of the centers of time-averaged fringes.

The approximated time-averaged moiré grating (Eq. (26)) and its graphical representation are depicted in parts (f)–(g) of Fig. 5. Black dashed lines throughout parts (d), (e), (f) and (g) indicate the centers of time-averaged fringes. It can be clearly seen that the centers of time-averaged fringes in parts (d)–(g) of Fig. 5 coincide, what confirms that approximated relationship (Eq. (26)) for the calculation of the time-averaged moiré grating can be used instead of Eq. (21).

3.3. The formation of time-averaged moiré fringes in 2D

Despite the fact that the obtained equations were derived for the one-dimensional case only, they still do hold for two-dimensional moiré gratings. Let us consider the 2D case. The position of the (i,j)-th point of the two-dimensional grating in the state of equilibrium reads:

$$x_{ij}(0) = L\tan\alpha_i \quad \text{and} \quad y_{ij}(0) = L\tan\gamma_j, \tag{28}$$

where α_i and γ_i are the angles between the incident laser beam and the lines connecting the DOE and the (i,j)-th point (Fig. 4).

The coordinates of the (i,j)-th point of the moiré grating at time moment t are calculated as follows:

$$x_{ij}(t) = L\tan\left(\alpha_i + \beta\sin\omega t\right) \quad \text{and} \quad y_{ij}(t) = \frac{L\tan\gamma_j\cos\alpha_i}{\cos\left(\alpha_i+\beta\sin\omega t\right)}. \tag{29}$$

Fig. 6 illustrates three states of the target image in the projection plane. The target image containing the 2D moiré grating in the state of equilibrium is shown in the middle; target images at maximal torsional deflections of the MEMS component are shown on the left and on the right sides. It is clear that the target image in the projection plane is deformed along the x- and the y-axis during the process of the torsional oscillation. The magnitude of deformation (in the projection plane) depends on many factors including β, L, and the structure of the CGH. The deformations along x-axis are accounted by Eq. (29) — in fact this behavior is the foundation of the proposed optical scheme. Really, deformations along the y-axis can be disregarded due to the reason that the lines of the moiré grating are parallel to the y-axis. Such an optical effect is inherent to any geometric moiré grating comprised from an array of parallel lines. In other words, optical geometric moiré techniques are insensitive to deformations in the direction of the constitutive grating lines [2].

4. Results

Let us consider a rectangular cover image in the projection plane. As mentioned previously, we aim to generate such cover image which would represent a 2D moiré grating. An ideal 2D moiré grating ($\lambda = 0.1$) is represented in Fig. 7(a). The phase structure of the CGH produced by adaptive–additive algorithm is illustrated in Fig. 7(b). The coherent illumination of the CGH by a laser beam produces the desired target image in the projection plane. The target image in the state of equilibrium (at $\beta = 0$) is depicted in Fig. 7(c). Note that the target image is contaminated by granular additive noise due to the iterative process of the adaptive–additive algorithm.

Computational experiments are continued in two directions. First of all we use the pure geometric scheme and do not involve the transformations induced by the CGH. Note that the frequency of oscillations does not have any influence on the formation of the time-averaged image (Eq. (26)) — if only the exposure time is much longer than the period of oscillations. This aspect is automatically resolved in our optical setup because time-averaged images are registered using conventional optical cameras, while microdevices are available over an extremely wide frequency range. Three different values of β are selected for the computational simulation of theoretical relationships — $\beta = 0.8, 0.9$ and 1.0 degrees. Time-averaged patterns of moiré fringes at respective values of β are depicted in Fig. 7(d), (e) and (f).

Virtual optical experiments are continued with the CGH at the same values of β — the results are illustrated in Fig. 7(g), (h) and (i). As noted previously, the derived theoretical relationships do approximate complex optical processes rather well at small angles of β. The same observation holds true in Fig. 7.

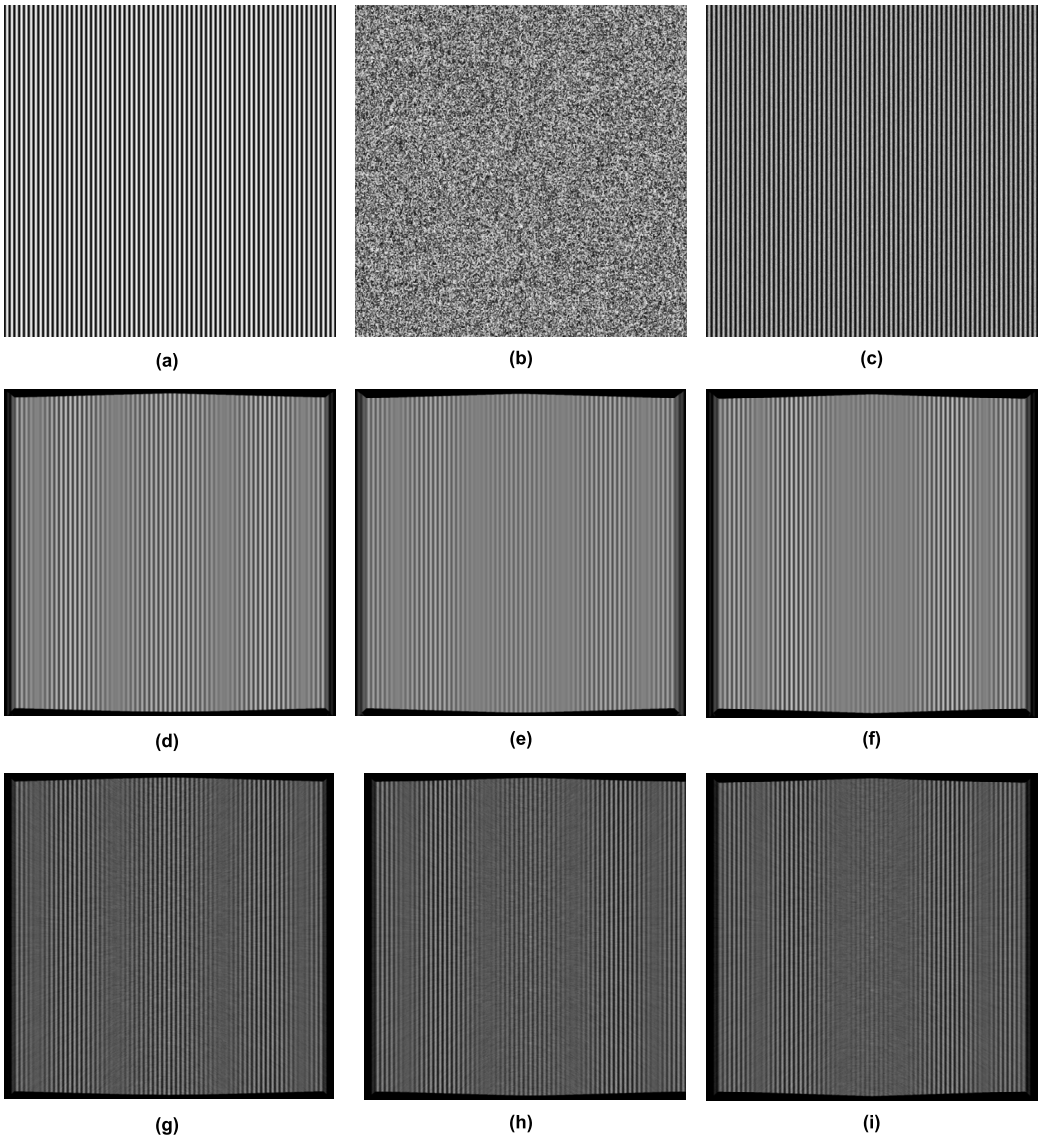

Fig. 7. Formation of interference fringes: (a) Moiré grating in the state of equilibrium. (b) Phase data of the DOE. (c) Moiré grating in the state of equilibrium on the projection plane. (d)–(f) Time-averaged images corresponding to moiré grating in part (a) with torsional amplitude equal $\beta = 0.8°$, $\beta = 0.9°$, $\beta = 1°$ respectively and $L = 2$, $\lambda = 0.1$. (g)–(i) Time-averaged images corresponding to moiré grating in part (c) with torsional amplitude equal $\beta = 0.8°$, $\beta = 0.9°$, $\beta = 1°$ respectively and $L = 2$, $\lambda = 0.1$.

It is clear that the ability to interpret moiré fringes in a time-averaged image builds a strong foundation for development of an optical sensor for the degradation prediction of MEMS components performing torsional oscillations. The principle of operation of such a sensor is illustrated in Fig. 8. Automatic or semi-automatic fringe counting techniques [2] should be used for the identification of time-averaged moiré fringes corresponding to the first root of J_0 – if they are only visible in the present observation window (for example, no time-averaged fringes are produced at all at $\beta = 0$). Then the centerline of the identified fringe should be used as a reference for further monitoring action. If the amplitude of torsional oscillations of the MEMS component will slowly change in time due to its mechanical or chemical degradation — the geometric location of the centerline in the projection plane will change too. The principal of such optical monitoring scheme is illustrated in Fig. 8.

The actual relationship between the position of the centerline of the first time-averaged fringe and the amplitude β is accurately determined by derived theoretical relationships. The sensitivity of such optical monitoring system can be easily adjusted by changing the dimensions of the optical setup (of course, neither the MEMS element nor the CGH need to be altered). Moreover, note that time-averaged images can be contrast-adjusted using automatic image processing algorithms [32] and may enhance the functionality of the monitoring system (Fig. 8).

Note that the location of the center of a time-averaged fringe produced by classical time-averaged geometric moiré is defined by Eq. (8) [1], but the location of the center of a time-averaged fringe produced by the proposed technique is completely different (Eq. (27)). Thus, it is clear that direct comparison of the time-averaged fringe patterns of classical time-averaged geometric moiré technique (Fig. 1(f)) and patterns produced by the proposed technique (Fig. 5(e,g), Fig. 7(d,e,f)) is not feasible — classical time-averaged geometric moiré is capable to estimate amplitudes of in-plane oscillations while the proposed technique estimates amplitudes of torsional out-of-plane oscillations. Moreover, classical time-averaged geometric moiré does not employ the CGH component which plays a pivotal role in the proposed optical setup Fig. 7(g,h,i)).

On the other hand the proposed optical setup is completely different from the technique designed for degradation prediction of mechanical components performing angular in-plane oscillations [6]. The major difference is that the technique presented in [6] is not oriented for MEMS systems, and therefore does not incorporate the CGH component. Moreover, in-plane angular oscillations allow direct optical integration

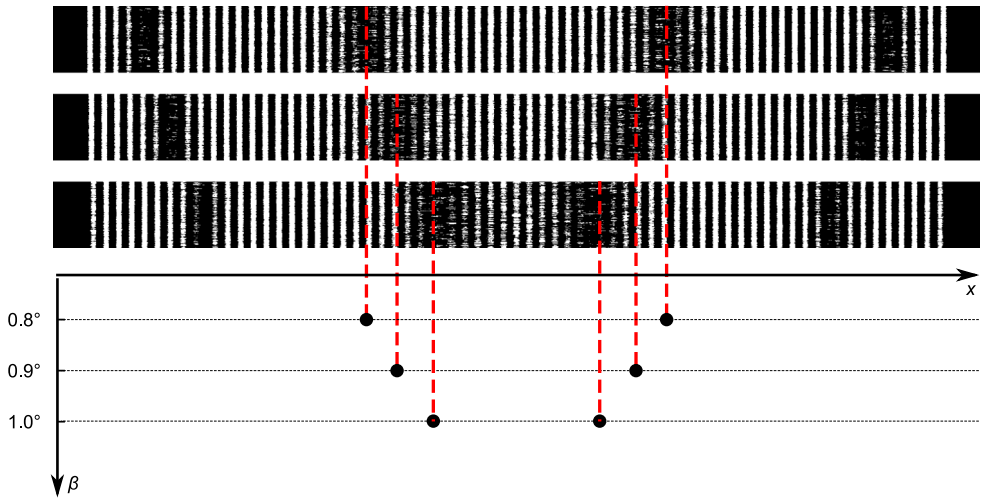

Fig. 8. The principal scheme of operation of an optical system for the degradation prediction of MEMS components performing torsional oscillations. Centerlines of contrast enhanced time-averaged fringes do track the variation of the amplitude of torsional oscillations of the MEMS component.

and result into a straightforward inverse problem — what is in a direct contrast to the presented optical technique.

5. Conclusions

In this paper the optical technique for the measurement of MEMS components performing torsional oscillations is presented. The proposed optical scheme is constructed by integrating time-averaged geometric moiré and CGH in such a way, that different amplitudes of torsional oscillations of MEMS components yield fringes at different locations in the projection plane. Furthermore, this approach enables the construction of optical sensor systems for the validation of MEMS components when the amplitude of torsional oscillations experience fluctuations due to changing environmental conditions or mechanical degradation. The significant advantage of the proposed approach is based on the fact that this is a pure optic technique allowing direct interpretation of dynamic behavior of MEMS components.

Acknowledgments

The authors appreciate the financial help provided by the Research, Development and Innovation Fund of Kaunas University of Technology (Grant No. PP32/1813) and the Jiangsu Provincial Recruitment Program of Foreign Experts (Type B, Grant 172 no. JSB2017007)

References

[1] A. Kobayashi, Society for experimental mechanics (U.S.), in: Handbook on Experimental Mechanics, VCH, 1993.
[2] K. Patorski, Handbook of the Moiré Fringe Technique, Elsevier, 1993.
[3] D. Post, B. Han, P. Ifju, High Sensitivity Moiré: Experimental Analysis for Mechanics and Materials, Springer-Verlag New York, 1994.
[4] F. Dai, Z. Wang, Geometric micron-moiré, Opt. Lasers Eng. 31 (3) (1999) 191–198.
[5] C. Liang, Y. Hung, A. Durelli, J. Hovanesian, Time-averaged moire method for in-plane vibrational analysis, J. Sound Vib. 62 (2) (1979) 267–275.
[6] P. Palevicius, A. Aleksa, R. Maskeliunas, M. Ragulskis, Circular geometric moiré for degradation prediction of mechanical components performing angular oscillations, Mech. Syst. Signal Process. 86 (2017) 278–285.
[7] G. Lebanon, A.M. Bruckstein, Energy Minimization Methods in Computer Vision and Pattern Recognition: Third International Workshop, EMMCVPR 2001 Sophia Antipolis, France, September 3–5, 2001 Proceedings, Springer Berlin Heidelberg, Berlin, Heidelberg, 2001, pp. 185–200,
[8] M. Naor, A. Shamir, Visual Cryptography, in: Lecture Notes in Computer Science, vol. 950, Springer-Verlag, 1995, pp. 1–12.
[9] X. Yan, S. Wang, X. Niu, C.-N. Yang, Halftone visual cryptography with minimum auxiliary black pixels and uniform image quality, Digit. Signal Process. 38 (2015) 53–65.
[10] X. Yan, S. Wang, X. Niu, C.-N. Yang, Generalized random grids-based threshold visual cryptography with meaningful shares, Signal Process. 109 (2015) 317–333.
[11] M. Ragulskis, A. Aleksa, Image hiding based on time-averaging moire, Opt. Commun. 282 (14) (2009) 2752–2759.
[12] G. Lu, L. Saunoriene, S. Aleksiene, M. Ragulskis, Optical image hiding based on chaotic vibration of deformable moiré grating, Opt. Commun. 410 (2018) 457–467.
[13] L. Saunoriene, S. Aleksiene, R. Maskeliunas, M. Ragulskis, Image hiding scheme based on time-averaged elliptic oscillations, Opt. Lasers Eng. 98 (2017) 83–88.
[14] D. O'Shea, T. Suleski, S. of Photo-optical Instrumentation Engineers, A. Kathman, D. Prather, Diffractive Optics: Design, Fabrication, and Test, in: Spie Press Monograph, Society of Photo Optical, 2004.
[15] W. Dallas, A. Lohmann, Holography, techniques — Computer-generated holograms, in: R.D. Guenther (Ed.), Encyclopedia of Modern Optics, Elsevier, Oxford, 2005, pp. 72–79.
[16] J. Turunen, Diffractive Optics for Industrial and Commercial Applications, Akademie Verlag, Berlin, 1997.
[17] D.C. Smith, Testing diamond turned aspheric optics using computer-generated holographic (CGH) interferometry, in: C.L. Stonecypher (Ed.), Contemp. Methods Opt. Fabr. (1982).
[18] F. Quentel, J. Fieret, A.S. Holmes, S. Paineau, Multilevel diffractive optical element manufacture by excimer laser ablation and halftone masks, in: M.C. Gower, H. Helvajian, K. Sugioka, J.J. Dubowski (Eds.), Laser Appl. Microelectron. Optoelectron. Manuf. VI (2001).
[19] J.M. Teijido, H. Buczek, D. Wuthrich, Manufacturing computer-generated holograms (CGH) by electron-beam, Microelectron. Eng. 9 (1–4) (1989) 255–257.
[20] R.W. Gerchberg, W.O. Saxton, A practical algorithm for the determination of the phase from image and diffraction plane pictures, Optik 35 (1972) 237–246.
[21] E.R. Dufresne, G.C. Spalding, M.T. Dearing, S.A. Sheets, D.G. Grier, Computer-generated holographic optical tweezer arrays, Rev. Sci. Instrum. 72 (3) (2001) 1810.
[22] S. Gu-Stoppel, J. Janes, D. Kaden, H.J. Quenzer, U. Hofmann, W. Benecke, Piezoelectric resonant micromirror with high frequency and large deflection applying mechanical leverage amplification, Proc. SPIE 8612 (2013) 8612–8612–8.
[23] T. Naono, T. Fujii, M. Esashi, S. Tanaka, A large-scan-angle piezoelectric MEMS optical scanner actuated by a Nb-doped PZT thin film, J. Micromech. Microeng. 24 (1) (2014) 15010.
[24] T. Izawa, T. Sasaki, K. Hane, Scanning micro-mirror with an electrostatic spring for compensation of hard-spring nonlinearity, Micromachines 8 (8) (2017).
[25] A. Caspani, C. Comi, A. Corigliano, G. Langfelder, V. Zega, S. Zerbini, Dynamic nonlinear behavior of torsional resonators in MEMS, J. Micromech. Microeng. 24 (9) (2014) 95025.
[26] L. Long, S. Zhong, A MEMS torsion magnetic sensor with reflective blazed grating integration, J. Micromech. Microeng. 26 (7) (2016) 75004.
[27] S.C. Charandabi, H.B. Muhammad, C.J. Anthony, P.D. Prewett, Development of a torsional paddle microresonator for mass detection, in: 2012 12th IEEE International Conference on Nanotechnology, IEEE-NANO, 2012, pp. 1–5.

[28] Z. Liu, X. Lou, J. Gao, Deformation analysis of MEMS structures by modified digital moir methods, Opt. Lasers Eng. 48 (11) (2010) 1067–1075, Micro and Nano Metrology in Experimental Mechanics.

[29] H. Wang, W. Yue, Q. Song, J. Liu, G. Situ, A hybrid Gerchberg–Saxton-like algorithm for DOE and CGH calculation, Opt. Lasers Eng. 89 (2017) 109–115, 3DIM-DS 2015: Optical Image Processing in the context of 3D Imaging, Metrology, and Data Security.

[30] R. Palivonaite, A. Aleksa, M. Ragulskis, Visual cryptography based on optical image projection, in: K. Elleithy, T. Sobh (Eds.), Innovations and Advances in Computer, Information, Systems Sciences, and Engineering, Springer New York, New York, NY, 2013, pp. 431–441.

[31] M. Ragulskis, Z. Navickas, Time average geometric Moiré—back to the basics, Exp. Mech. 49 (4) (2009) 439–450.

[32] M. Ragulskis, A. Aleksa, R. Maskeliunas, Contrast enhancement of time-averaged fringes based on moving average mapping functions, Opt. Lasers Eng. 47 (7) (2009) 768–773.